

Xenon-gas ionization chamber to improve particle identification of heavy ion beams with $Z > 70$

Masahiro Yoshimoto^{a,*}, Naoki Fukuda^a, Riku Matsumura^b, Daiki Nishimura^c, Hideaki Otsu^a, Yohei Shimizu^a, Toshiyuki Sumikama^a, Hiroshi Suzuki^a, Hiroyuki Takahashi^c, Hiroyuki Takeda^a, Junki Tanaka^a, Koichi Yoshida^a

^aRIKEN Nishina Center, 2-1 Hirosawa, Wako, Saitama 351-0198, Japan

^bSaitama University, 255 Shimo-Okubo, Sakura-ku, Saitama-shi, Saitama 338-8570 Japan

^cTokyo City University, 1-28-1 Tamazutsumi, Setagaya-ku, Tokyo 158-8557, Japan

Abstract

In conventional ionization chambers (ICs) using P-10 (Ar+CH₄) gas, as the atomic number (Z) of the ion beams increases in the energy region of 200–300 MeV/u, the Z resolution deteriorates rapidly when $Z > 70$. This degradation is attributed to substantial energy loss straggling caused by charge-state fluctuation when the beams traverse a gas medium. The energy loss straggling increases when the beams cannot attain charge-state equilibrium in the IC gas. In this study, a xenon-based gas (Xe+CH₄), exhibiting a sufficiently large charge-state changing cross section, was used in the IC to reach charge-state equilibrium. The responses of ICs with P-10 and the xenon-based gases were examined using ²³⁸U beams and cocktail radioactive isotope (RI) beams with $Z = 40$ –90 at the RI Beam Factory (RIBF). For ²³⁸U beams at 165–344 MeV/u, the P-10 gas IC yielded an energy resolution of 1.9–3.0% in full width at half maximum (FWHM), which proved inadequate for Z identification in the uranium region. In contrast, the xenon-based gas IC demonstrated a satisfactory energy resolution of 1.4–1.6%. When using cocktail RI beams, a Z resolution of 1.28 and 0.74 was achieved by the P-10 and the xenon-based gas ICs, respectively, for beams with $Z = 84$ –88 at 200 MeV/u. The contrast in Z resolutions between the P-10 and the xenon-based gas ICs was effectively elucidated by the energy loss straggling model, incorporating collisional straggling and straggling due to charge-state changes in the IC gases. The xenon-based gas IC, with more than 3σ Z separation across a broad Z range ($Z = 40$ –90), emerged as a practical solution for Z identification of heavy ion beams.

Keywords: Ionization chamber; Xenon gas; Heavy ion; Particle identification

1. Introduction

Radioactive isotope (RI) beams are appropriate for studying short-lived unstable nuclei. These beams are produced through in-flight fission or projectile fragmentation of energetic primary beams comprising stable

*Corresponding author

Email address: masahiro.yoshimoto@riken.jp (Masahiro Yoshimoto)

heavy ions. Objective RIs are subsequently separated and identified using in-flight RI-beam separators; these RIs are then used for experimental purposes. Since 2007, the RI Beam Factory (RIBF) has been a world-leading facility producing various RI beams at 200–300 MeV/u [1, 2]. Primary beams of ^{238}U , ^{124}Xe , ^{78}Kr , ^{70}Zn , ^{48}Ca , etc. are accelerated to 345 MeV/u by a Superconducting Ring Cyclotron (SRC) [1]; subsequently, RI beams are produced, separated, and identified in the BigRIPS separator [2]. A total of 171 new isotopes with a wide range of atomic numbers (Z) from 11 to 68 [3]–[16] have been discovered at RIBF; moreover, the neutron dripline for F and Ne has been determined [17]. Additionally, many other experiments based on inverse kinematics, such as Refs. [18, 19, 20] have been conducted.

The identification of RI beams involves deducing their atomic numbers (Z) and mass-to-charge ratios (A/Q) on an event-by-event basis. This is achieved through a TOF- $B\rho$ - ΔE (TOF; time-of-flight, $B\rho$; magnetic rigidity, and ΔE ; energy loss) method utilizing beamline detectors in BigRIPS [21]. TOF is measured using plastic scintillators; $B\rho$ values are determined through trajectory reconstruction from tracks measured using position-sensitive parallel plate avalanche counters (PPACs) [22]; and ΔE is measured using a multi-sampling ionization chamber (MUSIC, hereafter IC) [23, 24]. This particle-identification (PID) method has been successfully utilized to produce RI beams in the $Z < 70$ region at RIBF. Recently, heavier RI beams with $Z > 70$ have been produced using the projectile fragmentation of the ^{238}U primary beam, giving rise to the following issues [25, 26, 27]: (1) Neutron-rich RI beams face challenges in achieving sufficient separation from lower- Z contaminants produced through secondary reactions in energy degraders. (2) Yields of RI beams experience a drastic reduction during the separation and particle identification (PID) processes, which involve alterations in charge states at the beamline detectors and the energy degraders. (3) A higher A/Q resolution is essential due to the denser A/Q spectrum resulting from larger Q and the presence of multiple charge states. (4) Z resolution deteriorates in the IC with the widely-used P-10 (90% Ar + 10% CH₄) gas. At RIBF, Sumikama *et al.* have partly overcome the PID issues by transporting only He-like ions in $^{208}_{86}\text{Rn}^{84+}$ setting at 185 MeV/u [25]. Single charge-state beams near $A/Q = 2.5$ require a separation of only $\delta Z = 2$ difference in the two-dimensional PID spectrum of Z vs. A/Q ; hence, even a P-10 gas IC with a low Z resolution of approximately one in FWHM can be used for Z identification. However, other RI beams with A/Q deviating from 2.5 and/or those with multiple charge states require a separation of $\delta Z = 1$ difference. Thus, our focus is on enhancing the Z resolution itself to effectively handle common heavy RI beams.

The Z resolution is affected by the variation of the energy loss, called ΔE straggling, in the IC gas. For heavy ion beams, a drastic increase in the ΔE straggling has been observed, which is caused by changes in the charge state, namely the electron-capture and electron-loss processes [28]. To address this concern, a thick P-10 gas IC with 800 mg/cm² was utilized at GSI [29] for Z identification of heavy RI beams around $Z = 80$ with 300 MeV/u. This method augments the number of charge-state changes, approaching charge-state equilibrium, which is the asymptotic average charge state attained after many charge-state changes.

Although this approach yields a satisfactory Z resolution, there is an energy loss of approximately 80 MeV/u in the thick IC, rendering it impractical for supplying RI beams for direct reaction experiments at RIBF. To increase the number of charge-state changes under the same energy loss, a xenon-based gas IC was proposed, offering a charge-state changing cross section approximately one order of magnitude larger than that of ICs with P-10 gas [30].

This study compares the Z resolution of the newly-proposed xenon-based gas IC for $Z = 40$ –92 beams to that of the conventional P-10 gas IC. Section 2 explains the effect of charge-state changes on energy resolution and Z resolution. Section 3 describes the structure of the proposed IC, electronics, and IC gases. Section 4 summarizes the ^{238}U beams and cocktail RI beams with $Z = 40$ –90 used to evaluate the energy resolution and Z resolution, respectively. The results for the energy resolution and Z resolution are presented in Section 5 and a discussion on the Z resolution using simulations of charge-state fluctuations is presented in Section 6. Each resolution is given in full width at half maximum (FWHM) throughout this paper unless specified otherwise.

2. Effect of charge-state changes on energy resolution and Z resolution

The degraded Z resolution for heavy ion beams at 200–300 MeV/u is due to enhanced ΔE straggling caused by charge-state changes [28]. The mean energy-loss rate (dE/dx) is a function of Q not Z ; thus, the ΔE value depends on the charge state of each event in the medium.

For fully-stripped ions, dE/dx follows the Bethe equation using Z and velocity (β) of the ions as

$$\frac{dE}{dx} = Z^2 \frac{4\pi e^4}{m\beta^2 c^2} n_e \left(\frac{1}{2} \ln \frac{E_m^2}{I^2} - \beta^2 + \Delta_{cor} \right), \quad (1)$$

where e is the elementary charge, m is the electron mass, c is the speed of light, n_e is the electron density, I is the mean excitation energy, E_m is the maximum energy transfer to a target electron in a single collision of the ion and a material atom, and Δ_{cor} is the various corrections term [31]. The collisional straggling (Ω_{col}) in energy loss is expressed as follows:

$$\frac{d\Omega_{col}^2}{dx} = Z^2 \frac{2\pi e^4}{m\beta^2 c^2} n_e E_m X_{LS}, \quad (2)$$

where X_{LS} is the correction term by Lindhard and Sørensen [31]. The collisional straggling is mainly caused by stochastic fluctuations in the number and energy of released high-energy electrons (δ -rays), which are emitted when the energy transfer is large. Because the IC gas at BigRIPS is sufficiently thin to use a constant β assumption, the mean energy loss of the fully-stripped ions (ΔE_{full}) is expressed as

$$\Delta E_{full} = \xi(\beta) L Z^2, \quad (3)$$

where $\xi(\beta)$ is obtained from the right-hand side of Eq. 1 excluding Z^2 , and L is the gas thickness. The Z value is obtained by solving Eq. 3 and the relative uncertainty of Z is half of the fluctuation of ΔE_{full} .

In the case of partially-stripped ions, dE/dx is derived from Eq. 1, in which Z is replaced by Q ($<Z$). The energy loss of the i -th ion (event no. i) with charge-state changes ($\Delta E_{cc}(i)$) is expressed as follows:

$$\Delta E_{cc}(i) = \xi(\beta) \sum_{j=0}^{N_{cc}(i)} L_j(i) q_j^2, \quad (4)$$

where $N_{cc}(i)$ is the number of charge-state changes of the i -th ion, and $L_j(i)$ is the thickness that the ion with charge q_j after j -times changes passes through in the IC gas. Moreover, $\Delta E_{cc}(i)$ is given with the ratio $F_q(i)$ of the combined thickness that the ion with charge q passes to the gas thickness L via the following expression:

$$\Delta E_{cc}(i) = \xi(\beta) L \sum_{q=1}^Z F_q(i) q^2, \quad (5)$$

where $\sum F_q$ is equal to one. Here, the mean energy loss of all ions (ΔE_{cc}) is less than ΔE_{full} . The fluctuation of ΔE_{cc} with each event, called charge-exchange straggling (Ω_{cc}), occurs when the charge-state distribution broadens and F_q varies with each event. The fluctuation of F_q depends on N_{cc} . The average N_{cc} (\bar{N}_{cc}) is expressed as follows:

$$\bar{N}_{cc} = \sum_{q=1}^Z \bar{F}_q \frac{L}{\lambda_q}, \quad (6)$$

where λ_q is the mean free path of an ion with charge q and \bar{F}_q is the mean existence probability of ions with charge q . In general, the charge-exchange straggling becomes large when ions prefer being partially stripped in the gas and \bar{N}_{cc} is inadequate to attain charge-state equilibrium.

To elucidate the collisional and charge-exchange straggling, Fig. 1 illustrates examples of simulated charge-state fluctuations and energy resolution ($R = 2.355\Omega/\Delta E_{cc}$) at 250 MeV/u. The charge-state fluctuations were simulated using a dedicated Monte Carlo code, with charge-state changing cross sections taken from the GLOBAL code [33]. The collisional straggling (Ω_{col}) is calculated using Eq. 2, whereas ΔE_{cc} and Ω_{cc} are calculated using Eq. 5. Figure 1 illustrates results for $^{100}_{40}\text{Zr}^{40+}$ beam in P-10 gas (a), $^{205}_{82}\text{Pb}^{82+}$ beam in P-10 gas (b), and $^{205}_{82}\text{Pb}^{82+}$ beam in Xe gas (c). The horizontal bars in the left figures display the charge-state changes in the gas by color. The right figures show the energy resolution as a function of gas length. The orange dashed-dotted lines indicate the energy resolution of the collisional straggling (R_{col}), and the green solid lines indicate the energy resolution of the charge-exchange straggling (R_{cc}). The blue dashed lines indicate the energy resolution of the total ΔE straggling (R_{total}), which was calculated by adding Ω_{col} and Ω_{cc} in quadrature. The black dotted lines indicate the relative ΔE_{cc} difference between Z and $Z - 1$ as follows:

$$\frac{\Delta E_{cc}(Z) - \Delta E_{cc}(Z - 1)}{\Delta E_{cc}(Z)}, \quad (7)$$

which represents the required energy resolution to separate Z at 2.355σ .

When the Zr^{40+} beam is injected into the 760-Torr P-10 gas as shown in Fig. 1(a), R_{cc} is sufficiently small. Thus, R_{total} is dominated by the collisional straggling. Here, R_{col} decreases as a function of $1/\sqrt{L}$

from the relationship between Eqs. 5 and 2. The charge-exchange straggling is small because the Zr ions prefer being fully stripped to being partially stripped. Most ions remain fully stripped (yellow) throughout the gas. Some ions become H-like ions (light green); however, these H-like ions immediately revert to fully-stripped ions within short flight distances, thereby rendering the charge-state distribution narrow. As presented in a previous publication [32], the energy loss resolution obtained by the P-10 gas ICs translates to a sufficient Z resolution for ions with $Z < 50$ at 200–300MeV/u.

When the Pb^{82+} beam is injected into the 760-Torr P-10 gas as shown in Fig. 1(b), R_{cc} affects R_{total} . The Pb^{82+} ions tend to capture electrons in the P-10 gas. Thus, many ions change to H-like or He-like (green) in the gas. Since the λ of the partially-stripped Pb ions is longer than that of the Zr ions, the H-like and He-like Pb ions pass through the gas as partially-stripped ions with longer flight distances. Only a few ions remain fully stripped until the end of their trajectory through the gas. The charge-state distribution widens, and F_q varies with each event, thereby resulting in large R_{cc} . The inadequate Z resolution for ions with $Z = 80\text{--}90$ using the P-10 gas has been observed in earlier studies [25, 26, 27] at RIBF.

Figure 1(c) shows a case in which the Pb^{82+} beam is injected into the Xe gas. The Xe gas pressure is adjusted to be 280 Torr to induce an energy loss equivalent to that of the P-10 gas. Thus, R_{col} is the same as the result obtained using the P-10 gas. The charge-state distribution in the Xe gas is broader than that in the P-10 gas. The charge-state changes occur many times because the λ of partially-stripped Pb ions in the Xe gas is approximately an order of magnitude shorter than that in the P-10 gas. The simulated \bar{N}_{cc} is 23 in the 40-cm Xe gas, which is sufficient to reach charge-state equilibrium, while \bar{N}_{cc} of 2.2 in the 40-cm P-10 gas is insufficient. Although the charge-state distribution in the Xe gas becomes broader than that in the P-10 gas, the fluctuation of F_q is smaller. Hence, R_{cc} is reduced as L increases. The Z separation is expected to be possible with the Xe gas longer than 44 cm.

The R_{cc} peak positions of the Pb^{82+} beam are $L=40$ cm for the P-10 gas and $L=5$ cm for the Xe gas. Both have an \bar{N}_{cc} value of approximately 2. When \bar{N}_{cc} is small, R_{cc} increases because the effect of the broadening charge-state distribution as \bar{N}_{cc} increases is dominant. When \bar{N}_{cc} exceeds 2, R_{cc} decreases because the effect of averaging the charge-state fraction F_q becomes dominant. The R_{cc} value is proportional to \sqrt{L} at $\bar{N}_{cc} < 2$ and $1/\sqrt{L}$ at $\bar{N}_{cc} > 2$, similar to R_{col} . A choice to use short ICs with the P-10 gas to reduce \bar{N}_{cc} and R_{cc} with the Pb^{82+} beam does not work because R_{col} becomes large. Another choice to use long ICs is also difficult at RIBF. To achieve the required energy resolution for the Pb^{82+} beam, 120-cm gas is required; however, this is not feasible with the BigRIPS layout.

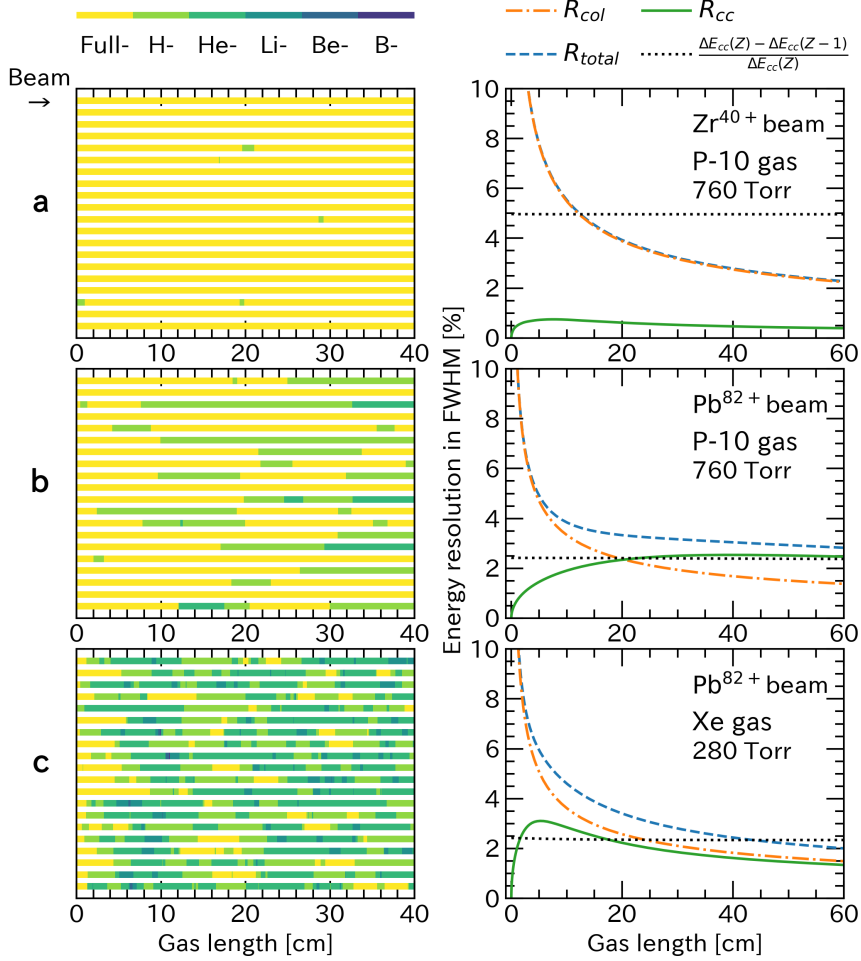


Figure 1: Simulations for charge-state fluctuation and energy resolution of (a) $^{100}\text{Zr}^{40+}$ into P-10 gas, (b) $^{205}\text{Pb}^{82+}$ into P-10 gas, and (c) $^{205}\text{Pb}^{82+}$ into Xe gas. The beam energy is 250 MeV/u. The pressure of the P-10 gas is 760 Torr, while that of the Xe gas is set at 280 Torr to achieve an equivalent ΔE . The horizontal bars in the left figures display the generated 20 events using the Monte Carlo method, and the color changes indicate the charge-state changes in the gas. The energy resolutions in the right figures were defined as $R = 2.355\Omega/\Delta E_{cc}$. The energy resolutions, R_{col} and R_{cc} were deduced with simulated collisional straggling using Eq. 2 and charge-exchange straggling using Eq. 5, respectively. The energy resolution with total ΔE straggling, R_{total} was estimated by adding the collisional and charge-exchange straggling in quadrature. The mean energy loss, ΔE_{cc} was estimated using the CATIMA energy loss calculator [34] and Eq. 5.

3. Development of the ionization chamber

3.1. Structure

A cross-sectional view of the newly-developed IC is shown in Fig. 2. This IC comprises 25 electrode planes aligned perpendicular to the beam axis. A total of 12 anodes and 13 cathodes are arranged alternately with 2.0-cm intervals. The active gas length is 48 cm. The electrodes are made of 2.5- μm thick aluminized Mylar films, supported by pairs of 1-mm thick aluminum rings with inner and outer diameters of 6.0 and 8.0 cm, respectively. The effective area is a circle with $\varnothing 6$ cm as uniform parallel electric fields are formed in the volume inside the inner diameters. This area is reduced from that of previous ICs [32, 35] comprising a circle of $\varnothing 23.2$ cm or a rectangle of 26×17 cm² because smaller electrodes may reduce the collisional straggling by exporting energy deposition of the high-energy δ -rays outside the active detection volume [36]. In addition, the smaller electrodes reduce capacitive noises. These electrodes are enclosed in an airtight aluminum chamber filled with IC gases. Upstream and downstream vacuum separation windows are 77- μm and 125- μm thick Kapton sheets, respectively, and their sizes are $\varnothing 7$ cm and $\varnothing 11$ cm, respectively. The distance between the windows is 60 cm. The inactive gas length from the upstream window to the first electrode is 1.6 cm, which is reduced from the 9.6 cm or 7.0 cm of previous ICs.

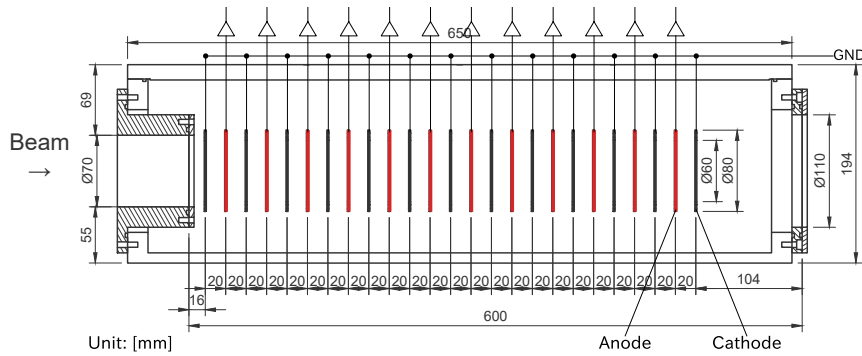


Figure 2: Cross-sectional view of the newly-developed multi-sampling ionization chamber. The red and black bold lines show 12 anodes and 13 cathodes, respectively, whose inner diameters are 6.0 cm. The active gas length is 48 cm.

3.2. Electronics

Ionization electrons originating from gas atoms are collected by the IC anodes under parallel electric fields that do not cause electron avalanches. A total of 12 output signals proportional to the energy deposit to each active volume are multi-sampled. Each signal was amplified by a preamplifier with 7- μs decay time and a shaping amplifier with 1- μs shaping time, and then processed by a 14-bit ADC. All 13 cathodes were grounded to the airtight aluminum chamber with copper wires. The preamplifiers were operated in vacuum and attached directly to the outside of the airtight chamber to reduce ground noise and stray capacitance. The 12 ADC values were geometrically averaged in the analysis to obtain ΔE .

3.3. Gases

The IC is filled with either the commonly-used P-10 gas (90% Ar + 10% CH₄) or the newly-proposed xenon-based gas (70% Xe + 30% CH₄). The gas pressures are controlled to be 620 Torr for both gases by the constraint of the gas-flow device. In the case of the P-10 gas, the active gas thickness is 61.2 mg/cm², and a voltage of +400 V is supplied to the anodes to maximize the electron drift velocity, estimated to be 4.9 cm/ μ s using Garfield++ [37]. For the Xe+CH₄ gas, the gas mixture ratio is set at 7:3, and the active gas thickness is 158 mg/cm². Although a higher percentage of xenon gas is desirable to take advantage of xenon properties on charge-state changing, it slows down the electron drift velocity, resulting in a broad signal waveform from the electrodes. This broadening causes an increase in pile-up events under high-rate beam conditions. Hence, a gas mixture ratio of 7:3 is adapted to maintain the same electron drift velocity as the P-10 case. A voltage of +800 V is supplied for the Xe+CH₄ gas in our experiment. Although a voltage of +1200 V was initially required to match the velocity of the P-10 gas, unforeseen discharge problems necessitated the use of the lower voltage, resulting in a calculated electron drift velocity of 3.5 cm/ μ s with the +800 V voltage.

The mean energy required to produce an electron-ion pair is 26 eV for the P-10 gas and 23 eV for the Xe+CH₄ gas. The number of initial electrons in the Xe+CH₄ gas increases by approximately 10% under the same energy loss condition, however, this increase is negligible for the improvement of the energy resolution. The energy loss exceeds 100 MeV in the IC gases for heavy RI beams with a typical energy of RIBF. The number of initial electrons is more than 10⁶, and thus its statistical fluctuation is less than 0.1%, which is sufficiently small to affect the energy resolution.

The energy loss of the Xe+CH₄ gas IC is approximately two times that of the P-10 gas IC under the same gas pressure used for our measurements. Because the estimated energy resolution with the collisional straggling (R_{col}) of the Xe+CH₄ gas IC is 0.7(= $1/\sqrt{2}$) times that of the P-10 gas IC, the Xe+CH₄ gas IC could achieve superior energy resolution and Z resolution in a low- Z region where Ω_{col} is dominant and Ω_{cc} is negligible. However, Z resolution did not improve in the low- Z region in our experiment. The cause of this phenomenon could be high-energy δ -rays escaping from the active detection volume, which is discussed in Section 6.

4. Experiment

The required range of RI beams for ICs in the BigRIPS separator spans up to $Z = 92$, encompassing energies of 150–300 MeV/u with multiple charge states. To evaluate the P-10 and Xe+CH₄ gas ICs, $^{238}_{92}\text{U}^{90+,91+}$ beams with an energy range of 165–344 MeV/u and cocktail RI beams with a wide Z range from 40 to 90 at 200–250 MeV/u were injected into the ICs.

4.1. ^{238}U beams

The ^{238}U beams were provided at energies of 344, 252, and 165 MeV/u with $Q=90+$ and $91+$. These charge states are widely used for heavy ion beams at a typical energy of 250 MeV/u at RIBF. The three energies were achieved by degrading the primary beam of 346.6-MeV/u $^{238}\text{U}^{86+}$ through a 0.2-mm thick plastic scintillator at BigRIPS focal plane F3, a 5-mm thick Be target at F0, and a 9-mm thick Be target at F0, respectively (see Fig. 3 for BigRIPS layout). These materials also served as electron strippers. The $90+$ or $91+$ ions were selectively filtered by slits at the momentum dispersive focal plane, F5. The ICs were positioned in the F7 chamber. For the determination of beam timings and trajectories into the ICs, a 0.1-mm thick plastic scintillator and two PPACs were installed in the F7 chamber. The sequence of detectors from upstream to downstream comprised the first PPAC, IC, second PPAC, and scintillator. To mitigate pile-up events, the beam intensity at F7 was regulated to approximately 1 kHz.

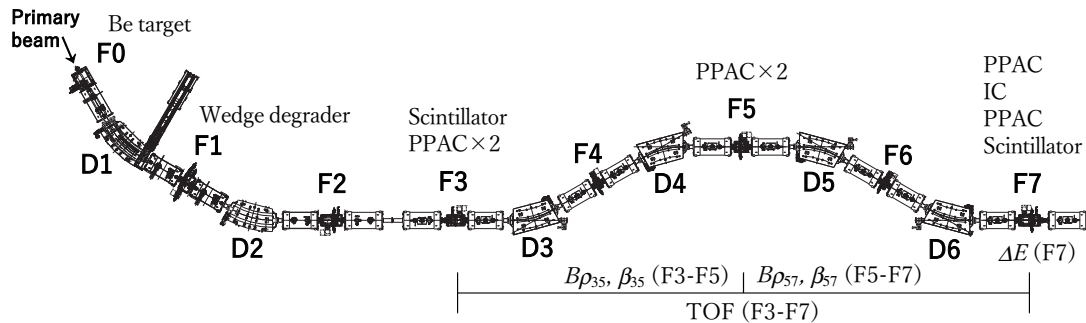


Figure 3: Layout of BigRIPS separator including focal planes, F0 to F7, and dipoles, D1 to D6. The combination of materials and detectors installed at each focal plane varies depending on the beam settings. The time of flight (TOF) is measured with the F3 and F7 plastic scintillators. Magnetic rigidity, $B\rho_{35}$ and $B\rho_{57}$, are determined through trajectory reconstruction with PPACs at F3, F5, and F7. Velocity, β_{35} and β_{57} are deduced by TOF and $B\rho$ values. The energy loss, ΔE is measured with the IC at F7.

4.2. Cocktail RI beams of $Z = 40-90$

The cocktail RI beams spanning $Z = 40-90$ were produced by the primary beam, $^{238}\text{U}^{86+}$, colliding with a 4-mm thick Be target at F0. The beams were then separated using the first dipole (D1) with a $B\rho$ of 6.1712 Tm and a 2-mm thick Al wedge energy degrader at F1. The $B\rho$ settings after F1 were adjusted

for the $^{210}\text{Rn}^{84+}$ beam, limiting the momentum width to $\pm 0.05\%$ by narrowing the F1 slit to ± 1 mm. For PID, the TOF between F3 and F7 was measured using 0.2-mm and 0.1-mm thick plastic scintillators, respectively. The $B\rho$ values were determined through trajectory reconstruction with PPACs installed at F3, F5, and F7. The A/Q and β values of each particle were deduced from the TOF and $B\rho$ values [21]. Considering partially-stripped ions, effective Q ($Q_{eff} = \sqrt{\sum F_q q^2} \leq Z$) instead of Z is derived from ΔE and β by using Eq. 5. In practice, the measured Q_{eff} was adjusted to Z using third-order polynomials. PID was further confirmed by detecting delayed γ rays emitted from the short-lived isomeric states of ^{138}Ba , ^{210}Rn , and ^{215}Ra [38]. The beam intensity was regulated to approximately 1 kHz at F7, consistent with one of the ^{238}U beams.

5. Results

5.1. ^{238}U beams

The energy-loss (ΔE) distributions of the $^{238}\text{U}^{90+,91+}$ beams at 344, 252, and 165 MeV/u measured by the P-10 and Xe+CH₄ gas ICs are illustrated in Fig. 4. The filled and open histograms depict the ΔE distributions of 90+ and 91+ ions, respectively. Table 1 provides a summary of the mean ΔE values, mean ΔE differences between 90+ and 91+, energy resolutions, and the average number of charge-state changes in the gas (\overline{N}_{cc}) at the equilibrium charge state calculated using Eq. 6.

The ΔE distributions of the $^{238}\text{U}^{90+,91+}$ beams at 344 MeV/u measured by the P-10 gas IC are presented in Fig. 4(a). A noticeable difference in the distribution between 90+ and 91+ is observed, where the mean ΔE of 91+ is 0.62% larger than that of 90+. The total thickness of the active gas and upstream substances is considerably thinner than the equilibrium thickness for 344-MeV/u ^{238}U beams, resulting in a mean ΔE dependence on the incident charge states. An asymmetric ΔE distribution for 90+ and a more symmetric distribution for 91+ were observed. This difference is caused by the gap between the incident charge states and the mean charge of 91.0+ at equilibrium in the gas. The high energy shoulder of the 90+ distribution is formed by the incident 90+ ions that were changed to 91+ in the gas. The 91+ distribution exhibits tails on both sides due to a portion of the incident 91+ ions converting to 90+ or 92+ ions. The energy resolutions are 3.0% for the 90+ and 2.9% for the 91+ ions. The required energy resolution for separating uranium ($Z = 92$) from protactinium ($Z = 91$) at 165–344 MeV/u is 2.1% calculated using Eq. 7. Considering the substantial mean ΔE difference of 0.62% and the inadequate energy resolutions of 3%, Z separation with the P-10 gas IC is unattainable in the uranium region at 344 MeV/u.

The ΔE distributions of the $^{238}\text{U}^{90+,91+}$ beams at 252 and 165 MeV/u, respectively, measured by the P-10 gas IC are presented in Figs. 4(b) and (c). As the energy decreases, the mean ΔE difference between 90+ and 91+ decreases, the energy resolutions improve, and the distributions of the two charge states become more similar and less asymmetric. The improvement at lower energies is attributed to an increase in mean

ΔE and a decrease in charge-exchange straggling due to the increase in \overline{N}_{cc} . Even with the energy reduced to 165 MeV/u, Z separation remains unattainable due to insufficient energy resolution and residual mean ΔE difference.

Figure 4(d) displays the ΔE distributions of the $^{238}\text{U}^{90+,91+}$ beams at 344 MeV/u measured by the Xe+CH₄ gas IC. The mean ΔE difference is 0.03%, which is negligible for the required energy resolution in the uranium region. The energy resolutions of 90+ and 91+ are both 1.6%, markedly better than those obtained by the P-10 gas IC. The distributions are nearly identical and symmetrical. Although the charge states near the upstream of the active gas depend on the incident charge states, the charge distribution quickly reaches equilibrium in the Xe+CH₄ gas, eliminating the incident charge-state dependence in the ΔE distribution. The Xe+CH₄ gas IC exhibits a negligible mean ΔE difference and superior energy resolutions compared to the 2.1% requirement, enabling Z separation in the uranium region even at 344 MeV/u.

The ΔE distributions of the $^{238}\text{U}^{90+}$ beams at 252 and 165 MeV/u, respectively, measured by the Xe+CH₄ gas IC are shown in Figures 4(e) and (f). Only the ΔE distributions of 90+ were measured as the difference in ΔE distributions between 90+ and 91+ is expected to be smaller at lower energies. The energy resolutions at 252 and 165 MeV/u are both 1.4%, enabling Z separation in the uranium region. Although the energy resolution at 165 MeV/u was anticipated to improve more than at 252 MeV/u due to the larger ΔE and \overline{N}_{cc} , no improvement was observed. This is attributed to columnar recombination occurring at high dE/dx conditions, as discussed in Section 6.

Table 1: Results of the ΔE distributions of the ^{238}U beams and calculated average number of charge-state changes (\overline{N}_{cc}). The required energy resolution is 2.1% for Z separation in the uranium region (see text).

IC gas	^{238}U energy [MeV/u]	Mean ΔE 90+ / 91+ [arb.unit]	Mean ΔE difference [%]	Energy resolution 90+ / 91+ [%]	\overline{N}_{cc}
P-10	344	186.42 / 187.57	0.62	3.0 / 2.9	1.7
	252	221.54 / 222.54	0.45	2.2 / 2.7	2.8
	165	289.05 / 289.40	0.12	1.9 / 2.1	7.8
Xe+CH ₄	344	406.70 / 406.83	0.03	1.6 / 1.6	23
	252	473.59 / -	-	1.4 / -	53
	165	601.57 / -	-	1.4 / -	175

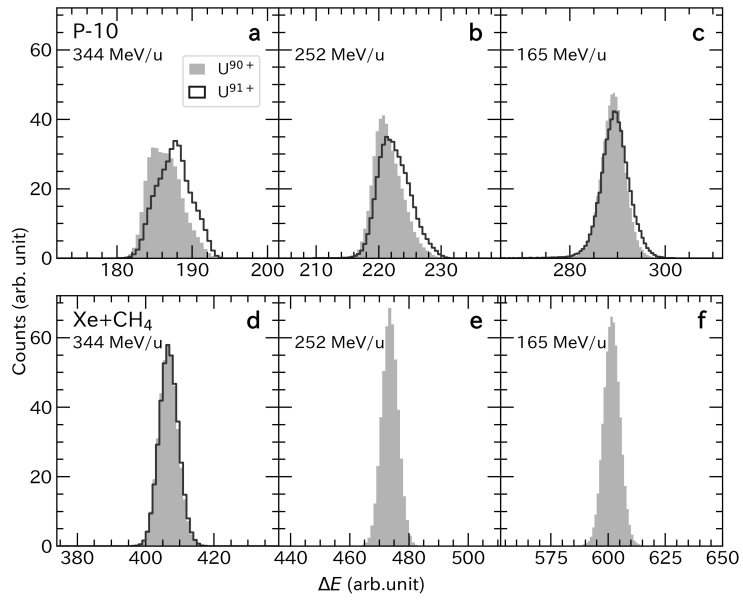


Figure 4: Energy loss (ΔE) distributions of ^{238}U beams at 344, 252, and 165 MeV/u measured by the P-10 and Xe+CH₄ gas ICs. The filled and open histograms represent the ΔE distributions of incident 90+ and 91+ ions, respectively. The horizontal axes of all spectra are scaled from 92% to 108% of the mean ΔE for comparison. The areas of all ΔE distributions are normalized to be equal.

5.2. Cocktail RI beams of $Z = 40\text{--}90$

The Z vs. A/Q PID plots for the cocktail RI beams of $Z = 40\text{--}90$ obtained with the P-10 and Xe+CH₄ gas ICs are depicted in Fig. 5. Ions with different Z , A , and Q are distributed as clusters in the PID plots, where Q represents the charge state between F3 and F7. The A/Q width of each cluster, A/Q resolution, obtained with the Xe+CH₄ gas IC (bottom) is inferior to that with the P-10 gas IC (top) due to poor TOF resolution caused by radiation damage to the plastic scintillator used for measurements with the Xe+CH₄ gas IC. The TOF resolutions of 140 ps and 170 ps were obtained for the P-10 and Xe+CH₄ gas ICs, respectively. This difference is negligible for Z resolution considering error propagation from β to ΔE . Subsequently, ions enclosed by the black solid lines are subject to analysis.

Figure 6 shows the incident energy at the entrance of the F7 chamber, calculated from β_{57} , as a function of Z . The mean energy decreases with increasing Z due to a larger energy loss for higher Z ions in the F1 energy degrader. The mean energy is 250.7 MeV/u at $Z = 40$ and 200.4 MeV/u at $Z = 88$.

The charge state of the ions in each cluster was identified using the condition that A , Q , and Z were integers. The ions in Group A were identified as fully-stripped ions because multiplying A/Q by Z resulted in integers. For Group B ions, clusters existed for which multiplying A/Q by Z resulted in integers and nonintegers. The former clusters were identified as fully-stripped ions and the subsequent clusters were identified as H-like ions because multiplying A/Q by $(Z - 1)$ resulted in integers. Fully-stripped ions ${}^AZ^{Z+}$ are adjacent to H-like ions ${}^A(Z+1)^{Z+}$ along the Z axis, as shown in the inset in Fig. 5 of the Xe+CH₄ gas IC. Because the pair of clusters, ${}^AZ^{Z+}$ and ${}^A(Z+1)^{Z+}$ in the P-10 gas IC cannot be separated, the clusters were considered equivalent to those in the Xe+CH₄ gas IC. Similarly, groups C and D were identified. Group C consists of H-like and He-like ions, whereas Group D comprises He-like ions.

Figure 7 displays the Z spectra. In the region of Group A, the Z peaks of the P-10 gas IC closely resemble those of the Xe+CH₄ gas IC. However, in the regions of groups B, C, and D, notable differences emerge: the Z peaks of the P-10 gas IC are lower and less distinct, whereas those of the Xe+CH₄ gas IC are separated up to $Z = 88$.

For the assessment of Z resolution in Group A, ribbon-shaped gates separating even- and odd- Z ions were applied (Fig. 8) to reveal tails hidden by neighboring peaks in the Z spectra. The black solid lines in Fig. 9 show the Z spectra of even- or odd- Z ions with exposed tails. The Z peaks of the Xe+CH₄ gas IC are symmetrical, whereas those of the P-10 gas IC at $Z = 59\text{--}70$ have low- Z tails. In both gases, the most probable charge state is fully stripped, with the fraction of H-like ions increasing with Z as shown in Fig. 10. For the P-10 gas, the \overline{N}_{cc} of 1.6–2.7 is small to reach charge-state equilibrium, resulting in the large charge-exchange straggling. The ions changing to H-like ions create low-energy tails in the ΔE_{cc} distribution, which also influence the Z distribution. Conversely, in the case of the Xe+CH₄ gas, the charge-exchange straggling is negligible for the collisional straggling because the \overline{N}_{cc} of 34–51 is sufficiently large. Consequently, symmetrical Z distributions are observed. The red dotted lines in Fig. 9 represent fitted

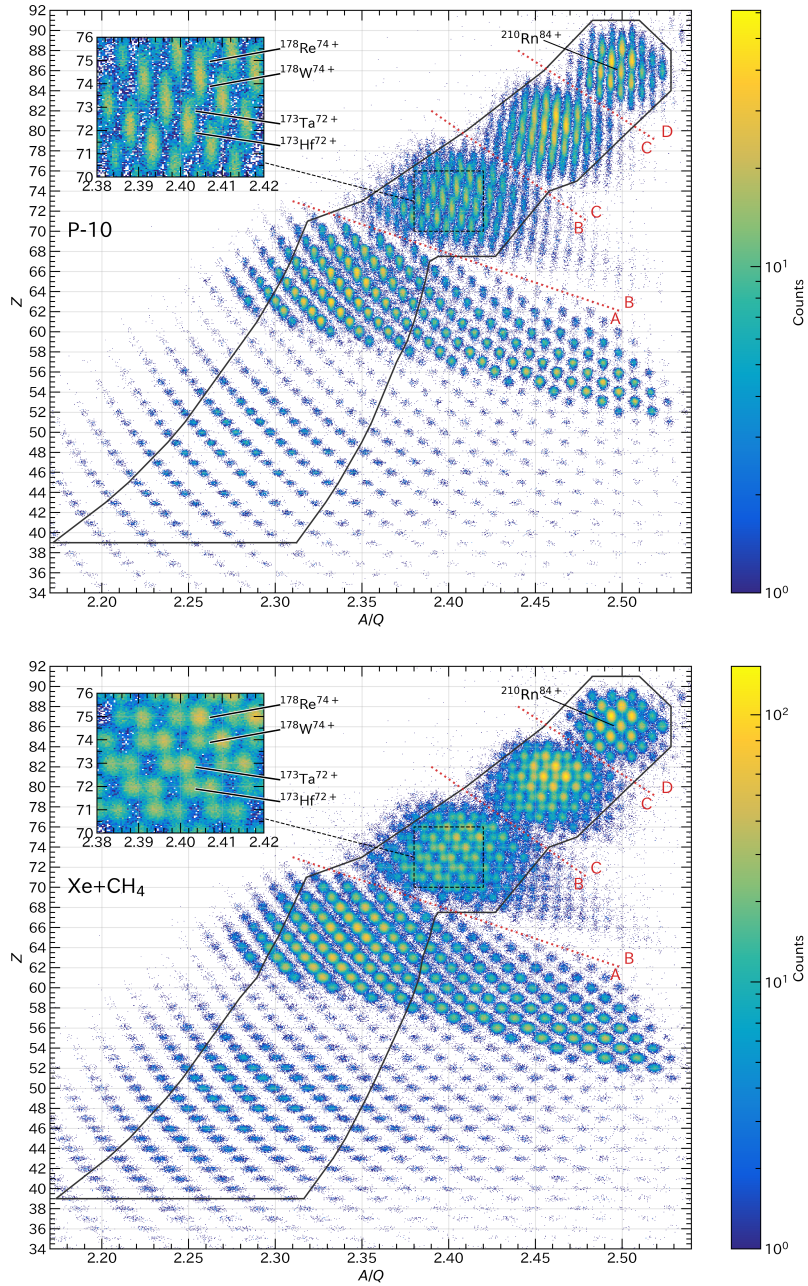


Figure 5: PID plots of Z vs. A/Q for the cocktail RI beams with $Z = 40\text{--}90$ injected into the P-10 (top) and Xe+CH₄ (bottom) gas ICs. The beam energy is 200–250 MeV/u and the particle on the central trajectory is ${}^{210}_{86}\text{Rn}^{84+}$. The red dotted lines show the boundaries of groups A, B, C, and D according to the charge states of the ions. The charge states in groups A, B, C, and D are fully stripped, a mixture of fully stripped and H-like, a mixture of H-like and He-like, and He-like ions, respectively. The charge state of the ions in each cluster was identified using the condition that A , Q , and Z were integers (see text). The black solid lines indicate two-dimensional gates for evaluation of the beam energy and Z resolution.

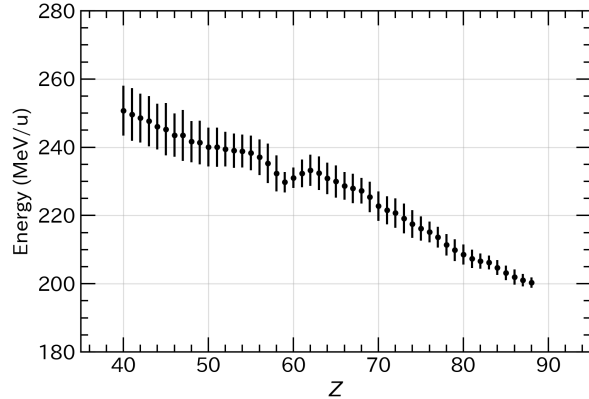


Figure 6: Incident energy of the cocktail RI beams of $Z = 40\text{--}90$ inside the two-dimensional gate in Fig. 5 as a function of Z . The incident energy at the entrance of the F7 chamber was calculated from β_{57} . The error bars indicate the standard deviation (SD). The mean energy is 250.7 (7.3 in SD) MeV/u at $Z = 40$ and 200.4 (1.5 in SD) MeV/u at $Z = 88$.

multiple skew normal functions representing tail components. The Z resolutions of the P-10 and Xe+CH₄ gas ICs are 0.45 and 0.44 at $Z = 50$, 0.69 and 0.64 at $Z = 62$, and 1.02 and 0.71 at $Z = 69$, respectively. The rapid deterioration of the Z resolution of the P-10 gas IC is attributed to the increased charge-exchange straggling.

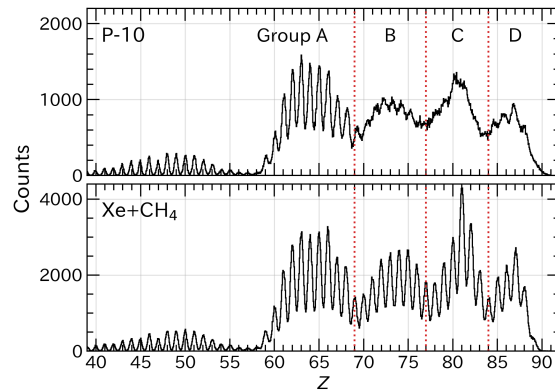


Figure 7: Z spectra of the cocktail RI beams inside the two-dimensional gates in Fig. 5 obtained with the P-10 and Xe+CH₄ gas ICs.

For groups B and C, separating even- and odd- Z ions was not possible owing to the dense PID spectrum. Figure 11 shows the Z spectra of all Z ions. The evaluation of Z resolution for the P-10 gas IC was not completed as the fully-stripped AZ^{Z+} and H-like $A(Z+1)^{Z+}$ ions, having the same A/Q value and different Z values, could not be separated. This difficulty is attributed not only to poor Z resolution but also to the mean ΔE_{cc} dependence on the incident charge states, similar to the ^{238}U -beam results of the P-10 gas

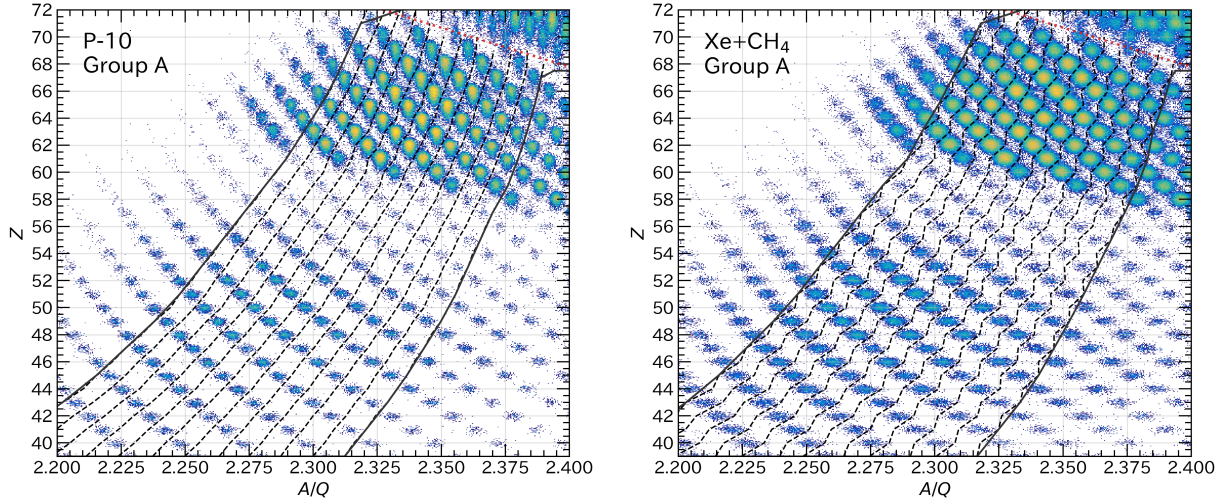


Figure 8: Example of ribbon-shaped gates indicated by dashed lines to divide the ions into even or odd Z for Group A of the cocktail RI beams. Gates for Group D are similar to those for Group A.

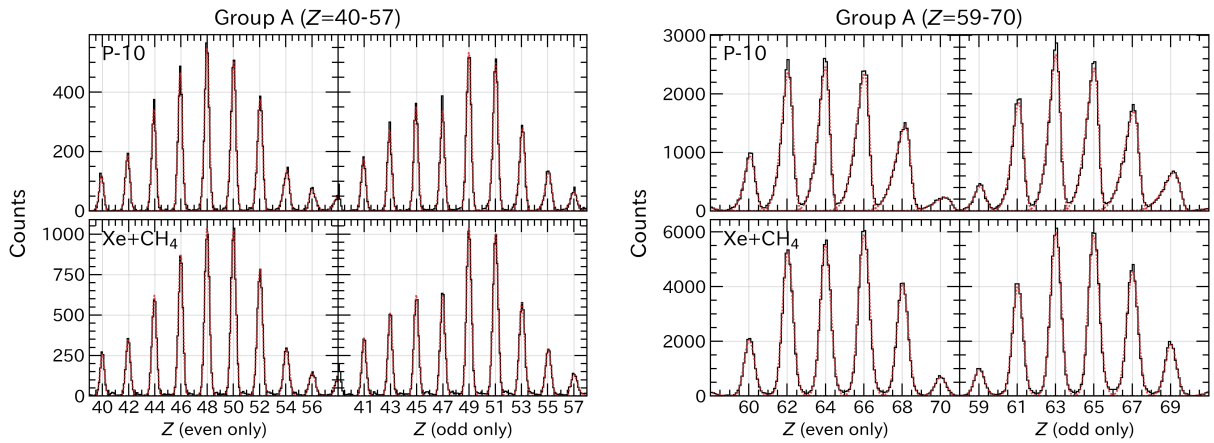


Figure 9: Z spectra of even- (left) or odd- Z (right) ions for Group A of the cocktail RI beams. The black solid lines show experimental data and the red dotted lines indicate the fitted skew-normal distributions.

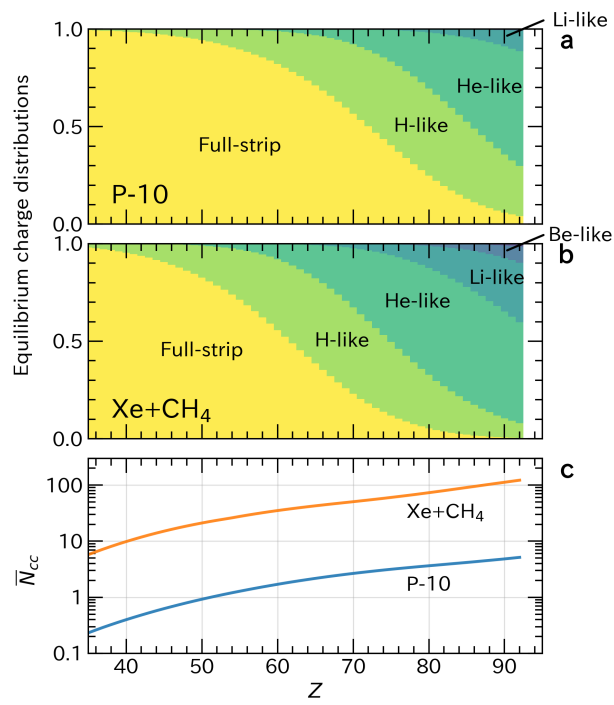


Figure 10: Calculated equilibrium charge distributions of the cocktail RI beams and the calculated average number of charge-state changes of the beam at the equilibrium charge state in the IC gas (\bar{N}_{cc}). The charge-state changing cross section is obtained from the GLOBAL code [33].

IC. In the case of the Xe+CH₄ gas IC, symmetrical Z peaks were observed. The Z distribution was fitted with multiple normal functions. The Z resolutions of the Xe+CH₄ gas IC were 0.69 at $Z = 74$ in Group B and 0.68 at $Z = 81$ in Group C. The Z resolutions of the Xe+CH₄ gas IC were almost constant within $Z = 70$ –84.

For Group D, consisting of He-like ions, Z resolution was evaluated as for Group A. The Z spectra of even- and odd- Z ions were separately analyzed (Figure 12). The high- Z tails of the P-10 gas IC were evaluated using multiple skew normal functions. The average Z resolutions of the P-10 and Xe+CH₄ gas ICs were 1.28 and 0.74 at $Z = 84$ –88, respectively. The worse Z resolution of the P-10 gas IC is attributed to the increased charge-exchange straggling.

The Z resolutions of all the groups are summarized in Fig. 13. The blue squares and orange circles denote the data obtained by the P-10 and Xe+CH₄ gas ICs, respectively. Both Z resolutions at $Z < 60$ were similar, while the Z resolutions of the Xe+CH₄ gas IC at $Z > 60$ were better than those of the P-10 gas IC. The Z resolution of the P-10 gas IC exceeded one at $Z > 70$, making it difficult to separate the $\delta Z = 1$ difference. In contrast, the Z resolution of the Xe+CH₄ gas IC was less than 0.8 and achieved a 3σ Z separation or better over a wide range of $Z = 40$ –90.

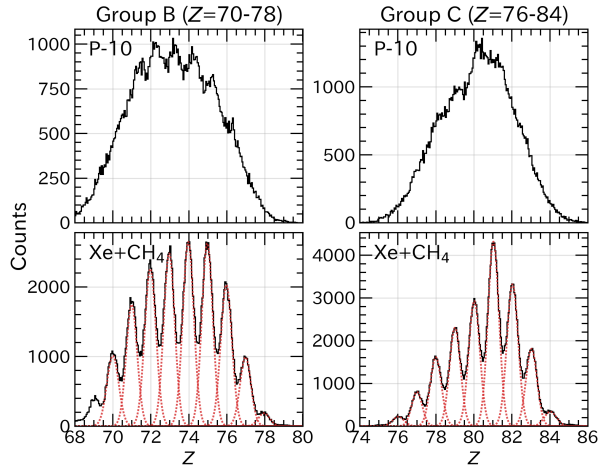


Figure 11: Z spectra of all Z ions in groups B (left) and C (right) of the cocktail RI beams. The black solid lines show experimental data and the red dotted lines indicate the fitted normal distributions. The Z spectra measured by the P-10 gas IC could not be fitted due to the unclear Z peaks.

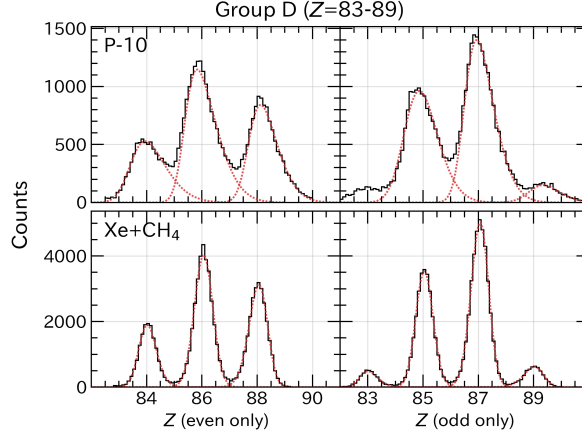


Figure 12: Z spectra of even- (left) and odd- (right) Z ions for Group D of the cocktail RI beams. The black solid lines show experimental data and the red dotted lines indicate the fitted skew-normal distributions.

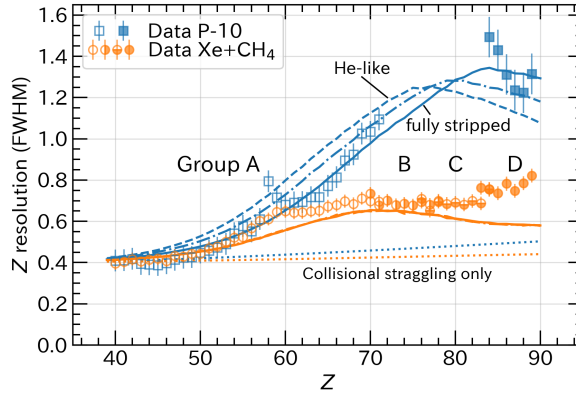


Figure 13: Z resolution of the cocktail RI beams with the P-10 and Xe+CH₄ gas ICs. The blue squares and orange circles represent the measured Z resolution (ΔZ_{data}) of the P-10 and Xe+CH₄ gas ICs, respectively. The filled styles of the symbols indicate groups A–D. The blue and orange lines depict the simulated Z resolution (R_{sim}) of the P-10 and Xe+CH₄ gas ICs, respectively. The dotted lines illustrate the Z resolution (ΔZ_{sim}^{colT}) assuming only collisional straggling, with the truncated energy of the δ -rays adopted to reproduce ΔZ_{data} of $Z = 40$ –50. The other lines depict the Z resolution including both collisional and charge-exchange straggling (ΔZ_{sim}^{total}). The solid, dashed-dotted, and dashed lines denote incident ions with fully-stripped, H-like, and He-like, respectively. The three lines for the Xe+CH₄ gas IC overlap each other due to nearly identical Z resolutions.

6. Discussion

6.1. Comparison with ΔE straggling model for Z resolution

The measured Z resolutions (ΔZ_{data}) by the P-10 and Xe+CH₄ gas ICs were compared using the ΔE straggling model, which includes collisional straggling and charge-exchange straggling, as explained in Section 2. The simulated Z resolution (ΔZ_{sim}) was derived from the simulated energy loss (ΔE_{sim}) and the simulated ΔE straggling (Ω_{sim}) as follows:

$$\Delta Z_{sim}(Z) = \frac{2.355\Omega_{sim}(Z)}{\Delta E_{sim}(Z) - \Delta E_{sim}(Z-1)}, \quad (8)$$

where 2.355 is the ratio of the FWHM to standard deviation. Note that ΔZ_{sim} in this definition is equivalent to ΔZ_{data} .

Both ΔZ_{data} values by the P-10 and Xe+CH₄ gas ICs were similar at $Z < 50$, although the Z resolution of the Xe+CH₄ gas IC is expected to be superior to that of the P-10 gas IC because of the double energy loss. Because the majority of the ions are fully stripped in the $Z < 50$ region, charge-exchange straggling has a limited effect on ΔE straggling. To interpret the similar Z resolutions in terms of the collisional straggling only, the truncated Bethe-Bohr model reported by Pfützner et al.[36] was used. In the model, high-energy δ -rays escaping from the active detection volume are considered. The decreased energy-loss rate (dE_{colT}/dx) and collisional straggling (Ω_{colT}) in the truncated Bethe-Bohr model are given by modifying Eqs. 1 and 2 as follows

$$\frac{dE_{colT}}{dx} = Z^2 \frac{4\pi e^4}{m\beta^2 c^2} n_e \left(\frac{1}{2} \ln \frac{E_m E_d}{I^2} - \beta^2 + \Delta_{cor} \right) \quad (9)$$

and

$$\frac{d\Omega_{colT}^2}{dx} = Z^2 \frac{2\pi e^4}{m\beta^2 c^2} n_e E_d X_{LS}, \quad (10)$$

respectively, with truncated δ -ray energy, E_d ($\leq E_m$) defined in Ref.[36], which corresponds to the maximum energy of δ -rays absorbed in the active detection volume. The simulated Z resolution (ΔZ_{sim}^{colT}) was derived from ΔE_{colT} and Ω_{colT} using Eq. 8.

The truncated δ -ray energy of E_d was determined such that ΔZ_{sim}^{colT} reproduces the ΔZ_{data} at $Z = 40$ – 50 for the cocktail RI beams in this study. For the Xe+CH₄ gas IC, a value of E_d equal to 620 keV was obtained. Given that the maximum δ -ray energy (E_m) is 620 keV for the 250-MeV/u cocktail RI beam at $Z = 40$, it is assumed that the entire range of δ -rays was detected in the active detection volume. In the case of the P-10 gas IC, E_d was determined to be 300 keV, approximately half of E_m . This twofold difference in E_d between the Xe+CH₄ and P-10 gas ICs can be attributed to the twofold difference in the energy-loss rate. In a previous study at RIBF [35], E_d of 310 keV was reported for cocktail RI beams of $Z = 40$ – 50 at approximately 330 MeV/u, measured with a similar P-10 gas IC. However, the electrode size in the previous IC was 26×17 cm², considerably larger than the present IC with a size of $\varnothing 6$ cm. Reference [36] suggested

that E_d is independent of the beam energy; however, it is reasonable to consider that E_d depends on the active detection volume. The similar E_d values obtained by ICs with different electrode sizes could be due to the simplistic approach of this model, as pointed out by Pfützner et al. [36], or the complex active detector volume, including support rings and electrode films. To investigate the dependence on the electrode size, additional experiments are required in which the same RI beams are injected into two ICs with different-size electrodes. In Fig. 13, the ΔZ_{sim}^{colT} values calculated up to $Z = 90$ using the obtained E_d values are shown by the dotted lines. The ΔZ_{sim}^{colT} values were nearly independent of Z . The ΔZ_{data} values at $Z > 50$ are considerably larger than ΔZ_{sim}^{colT} in both ICs, indicating the effect of the charge-exchange straggling.

In the Monte Carlo simulation of the charge-exchange straggling, the IC and upstream PPAC are taken into consideration. The charge-state changing cross section is obtained from the GLOBAL code [33], considering charge states from fully stripped to C-like. The ΔE_{cc} distribution is derived from Eq. 5, assuming a constant β in the gas. Simulated Z resolution, ΔZ_{sim}^{total} with collisional and charge-exchange straggling was derived using Eq. 8 from ΔE_{cc} and the total ΔE straggling (Ω_{total}), which is the width of the ΔE_{cc} distribution convoluted with Ω_{colT} .

The ΔZ_{sim}^{total} values with fully-stripped, H-like, and He-like incident ions are shown by the solid, dashed-dotted, and dashed lines in Fig. 13, respectively. There are two features of the P-10 gas IC. First, ΔZ_{sim}^{total} depends on the incident charge states. The cause of this dependence is the same as that of the difference in the ΔE distributions of $U^{90+,91+}$ beams, as shown in Fig. 4. The charge-state distributions in the P-10 gas IC depend on the incident charge state owing to the small \bar{N}_{cc} of <5 as shown in Fig. 10(c). Second, the incident charge state, which gives the best ΔZ_{sim}^{total} depends on Z . The fully-stripped ions give the best ΔZ_{sim}^{total} for $Z \leq 78$, whereas the He-like ions give the best ΔZ_{sim}^{total} for $Z \geq 79$. These preferable charge states approximately correspond to the most probable charge state, which is fully stripped for $Z \leq 74$ and He-like for $Z \geq 85$ as shown in Fig. 10(a). For the Xe+CH₄ gas IC, the ΔZ_{sim}^{total} values are independent of the incident charge states because of the large \bar{N}_{cc} of >20 at $Z > 50$, which is sufficiently large for the charge distribution to reach equilibrium near the upstream of the active gas.

The ΔZ_{sim}^{total} lines in Fig. 13 generally reproduce the ΔZ_{data} values for both ICs: they degrade with increasing Z , and their disparity between the P-10 and Xe+CH₄ gas ICs amplifies at $Z > 50$. This implies that ΔZ_{data} is reasonably explained by the ΔE straggling model. In more granular detail, the ΔZ_{data} values tend to be worse than the ΔZ_{sim}^{total} in the high- Z region for both ICs. For instance, the ΔZ_{data} values for the P-10 gas IC at $Z > 84$ appear to be worse than the ΔZ_{sim}^{total} line of the incident He-like ions, and those for the Xe+CH₄ gas IC at $Z > 80$ are inferior to the ΔZ_{sim}^{total} lines. Similar phenomena are observed in the energy resolutions of the ²³⁸U beams for the Xe+CH₄ gas IC. The energy resolution did not improve even as \bar{N}_{cc} increased with a decrease in the beam energy from 252 to 165 MeV/u, as described in Section 5.1. One plausible explanation for these disparities is columnar recombination. Columnar recombination takes place near the trajectory of high dE/dx beams, where the density of low-energy ionization electrons and

positive gas ions is extremely high. The recombination of the low-energy electrons and gas ions reduces the ΔE value, leading to a decrease in the mean ΔE difference between Z and $Z - 1$ ions. The measured ΔE at $Z > 70$ with the Xe+CH₄ gas IC is smaller than the ΔE_{cc} values in Eq. 5, although the other measured ΔE values with the P-10 and Xe+CH₄ gas IC are nearly reproduced by the calculated ones. Given that the dE/dx with the Xe+CH₄ gas IC is the largest in our measurements, this discrepancy could be attributed to columnar recombination. On the contrary, the collisional straggling is likely unaffected by columnar recombination, as high-energy δ -rays are spatially dispersed and less prone to recombine. Consequently, the Z resolution and energy resolution are expected to qualitatively worsen under high dE/dx conditions.

6.2. Perspective

The IC gases alter the charge distribution of heavy ion beams after passing through the ICs; however, this change does not affect inverse-kinematic nuclear-reaction experiments at RIBF. The beam position at F8, where secondary targets are located, remains independent of the charge state after F7 because these two focal planes are connected via a straight beamline without dipole magnets [2].

Notably, the Xe+CH₄ gas induces approximately two times the energy loss compared to the P-10 gas. For instance, the energy loss of ²¹⁰Rn at 250 MeV/u is 6.4 MeV/u when using the active gas length of the P-10 gas, whereas it is 13.7 MeV/u with that of the Xe+CH₄ gas. Despite this difference, it remains acceptable for most experiments conducted at RIBF. To further mitigate the energy loss induced by the Xe+CH₄ gas IC, the gas pressure can be reduced. Even if the gas pressure of the Xe+CH₄ is halved to achieve energy-loss equivalence with the P-10 gas IC, a sufficient \bar{N}_{cc} is maintained. This is due to the charge-state changing cross section of the Xe+CH₄ gas being one order of magnitude higher than that for the P-10 gas. Although the reduction in ΔE may lead to a degradation in Z resolution, a decreased truncated δ -ray energy (E_d) resulting from a lower energy-loss rate may compensate for the compromised Z resolution.

7. Summary

The Xe+CH₄ gas ionization chamber (IC) was developed to identify Z of heavy ion beams with $Z > 70$ at RIBF. To assess the energy and Z resolutions of both the commonly-used P-10 gas and the newly-proposed Xe+CH₄ gas ICs, ²³⁸U^{90+,91+} beams at 165, 252, and 344 MeV/u, and cocktail radioactive isotope (RI) beams with Z ranging from 40 to 90 at 200–250 MeV/u were injected into these ICs. Results from the ²³⁸U beam injected into the P-10 gas IC indicated difficulty in Z separation in the uranium region. This difficulty arises from a substantial difference in mean energy losses between U⁹⁰⁺ and U⁹¹⁺ beams, coupled with an energy resolution of 1.9–3.0% in FWHM, which is insufficient for the required 2.1% for Z separation in the uranium region. Conversely, results with the U beams in the Xe+CH₄ gas IC demonstrated sufficient performance for Z separation. The negligible mean energy-loss difference and an energy resolution of 1.4–1.6% were better than the required resolution of 2.1%. Results with the cocktail RI beams revealed that

the Xe+CH₄ gas IC exhibited a superior Z resolution compared to the P-10 gas IC at $Z > 65$. The FWHM of the Z resolution of the P-10 gas IC at $Z > 70$ was larger than 1, rendering Z separation challenging. In contrast, the Z resolution of the Xe+CH₄ gas IC was 0.69 at $Z = 67$ –70 and 0.74 at $Z = 84$ –88, proving sufficient for Z separation. With the Xe+CH₄ gas IC, 3σ Z separation or better was achieved in a wide Z region up to $Z = 90$. The difference in Z resolution at $Z > 65$ between the P-10 and Xe+CH₄ gas ICs was explained by simulated charge-exchange straggling, in addition to collisional straggling using the truncated Bethe-Bohr model. The Xe+CH₄ gas IC is suitable for Z identification of heavy ion beams with multi-charge states in the energy range 200–300 MeV/u, without a significant increase in the energy loss in the IC gas thickness. Therefore, the Xe+CH₄ gas IC considerably facilitates the production of heavy RI beams in RIBF and other facilities.

8. Acknowledgements

The authors acknowledge the staff of the RI Beam Factory. The experiments were conducted at the RI Beam Factory operated by RIKEN Nishina Center and the Center for Nuclear Study, University of Tokyo. This work was supported by the JSPS A3 Foresight Program, “Nuclear Physics in the 21st Century”. The authors would like to thank S. Kukita for his support of our theoretical understanding.

References

- [1] Y. Yano, Nucl. Instr. Meth. B 261 (2007) 1009–1013.
- [2] T. Kubo, D. Kameda, H. Suzuki, N. Fukuda, H. Takeda, Y. Yanagisawa, M. Ohtake, K. Kusaka, K. Yoshida, N. Inabe, T. Ohnishi, A. Yoshida, K. Tanaka, Y. Mizoi, Prog. Theor. Exp. Phys. 2012 (2012) 03C003.
- [3] T. Ohnishi, et al., J. Phys. Soc. Jpn. 77 (2008) 083201.
- [4] T. Ohnishi, et al., J. Phys. Soc. Jpn. 79 (2010) 073201.
- [5] B. Blank, et al., Phys. Rev. C 93 (2016) 061301.
- [6] I. Čeliković, et al., Phys. Rev. Lett. 116 (2016) 162501.
- [7] T. Sumikama, et al., Phys. Rev. C 95 (2017) 051601.
- [8] H. Suzuki, et al., Phys. Rev. C 96 (2017) 034604.
- [9] H. Suzuki, et al., Phys. Rev. Lett. 119 (2017) 192503.
- [10] N. Fukuda, et al., J. Phys. Soc. Jpn. 87 (2018) 014202.
- [11] Y. Shimizu, et al., J. Phys. Soc. Jpn. 87 (2018) 014203.
- [12] O.B. Tarasov, et al., Phys. Rev. Lett. 121 (2018) 022501.
- [13] K. Wimmer, et al., Physics Letters B 795 (2019) 266–270.
- [14] T. Sumikama, et al., Phys. Rev. C 103 (2021) 014614.
- [15] D.S. Ahn, et al., Phys. Rev. Lett. 129 (2022) 212502.
- [16] Y. Shimizu, et al., Phys. Rev. C, Accepted for publication.
- [17] D.S. Ahn, et al., Phys. Rev. Lett. 123 (2019) 212501.
- [18] H.L. Crawford, et al., Phys. Rev. Lett. 122 (2019) 052501.
- [19] R. Taniuchi, et al., Nature 569 (2019) 53–58.

- [20] S. Bagchi, et al., *Phys. Rev. Lett.* 124 (2020) 222504.
- [21] N. Fukuda, T. Kubo, T. Ohnishi, N. Inabe, H. Takeda, D. Kameda, H. Suzuki, *Nucl. Instr. Meth. B* 317 (2013) 323–332.
- [22] H. Kumagai, T. Ohnishi, N. Fukuda, H. Takeda, D. Kameda, N. Inabe, K. Yoshida, T. Kubo, *Nucl. Instr. Meth. B* 317 (2013) 717–727.
- [23] W.B. Christie, J.L. Romero, F.P. Brady, C.E. Tull, C.M. Castaneda, E.F. Barasch, M.L. Webb, J.R. Drummond, H.J. Crawford, I. Flores, D.E. Greiner, P.J. Lindstrom, H. Sann, J.C. Young, *Nucl. Instr. Meth. A* 255 (1987) 466–476.
- [24] K. Kimura, T. Izumikawa, R. Koyama, T. Ohnishi, T. Ohtsubo, A. Ozawa, W. Shinozaki, T. Suzuki, M. Takahashi, I. Tanihata, T. Yamaguchi, Y. Yamaguchi, *Nucl. Instr. Meth. A* 538 (2005) 608–614.
- [25] T. Sumikama, T. Kubo, N. Fukuda, D.S. Ahn, H. Takeda, Y. Shimizu, H. Suzuki, N. Inabe, D. Murai, H. Sato, K. Kusaka, Y. Yanagisawa, M. Ohtake, K. Yoshida, *Nucl. Instr. Meth. B* 463 (2020) 237–240.
- [26] N. Inabe et al., *RIKEN Accel. Prog. Rep.* 48 (2015) 73.
- [27] N. Fukuda, H. Suzuki, Y. Shimizu, H. Takeda, J. Tanaka, K. Yoshida, *RIKEN Accel. Prog. Rep.* 54 (2021) 81.
- [28] H. Weick, H. Geissel, C. Scheidenberger, F. Attallah, D. Cortina, M. Hausmann, G. Münzenberg, T. Radon, H. Schatz, K. Schmidt, J. Stadlmann, K. Sümmerer, M. Winkler, *Phys. Rev. Lett.* 85 (2000) 2725–2728.
- [29] L. Audouin, L. Tassan-Got, P. Armbruster, K.-H. Schmidt, C. Stéphan, J. Taieb, *Nucl. Instr. Meth. A* 548 (2005) 517–539.
- [30] T. Sumikama, N. Fukuda, M. Yoshimoto, *RIKEN Accel. Prog. Rep.* 56 (2023) S24.
- [31] J. Lindhard, A.H. Sørensen, *Phys. Rev. A* 53 (1996) 2443–2456.
- [32] Y. Sato, A. Taketani, N. Fukuda, H. Takeda, D. Kameda, H. Suzuki, Y. Shimizu, D. Nishimura, M. Fukuda, N. Inabe, H. Murakami, K. Yoshida, T. Kubo, *Jpn. J. Appl. Phys.* 53 (2014) 016401.
- [33] C. Scheidenberger, T. Stöhlker, W.E. Meyerhof, H. Geissel, P.H. Mokler, B. Blank, *Nucl. Instr. Meth. B* 142 (1998) 441–462.
- [34] CATIMA, <https://github.com/hrosiak/catima>
- [35] Y. Sato, N. Inabe, D. Kameda, T. Kubo, Y. Shimizu, H. Suzuki, H. Takeda, A. Taketani, D. Nishimura, N. Fukuda, M. Fukuda, H. Murakami, K. Yoshida, *RIKEN Accel. Prog. Rep.* 46 (2012) 159.
- [36] M. Pfützner, H. Geissel, G. Münzenberg, F. Nickel, Ch. Scheidenberger, K.-H. Schmidt, K. Sümmerer, T. Brohm, B. Voss, H. Bichsel, *Nucl. Instr. Meth. B* 86 (1994) 213–218.
- [37] Garfield++ CERN. <https://garfieldpp.web.cern.ch/garfieldpp/>
- [38] National Nuclear Data Center, information extracted from the NuDat database, <https://www.nndc.bnl.gov/nudat/>